Composites Part A 132 (2020) 105833

Contents lists available at ScienceDirect

Composites Part A

journal homepage: www.elsevier.com/locate/compositesa

Damage assessment of NCF, 2D and 3D woven composites under compression after multiple-impact using acoustic emission

Milad Saeedifar[a,1,*], Mohamed Nasr Saleh[a,1], Hassan M. El-Dessouky[b,c], Sofia Teixeira De Freitas[a], Dimitrios Zarouchas[a]

[a] Structural Integrity & Composites, Faculty of Aerospace Engineering, Delft University of Technology, Delft 2629 HS, The Netherlands
[b] Composite Centre, AMRC with Boeing, University of Sheffield, Rotherham S60 5TZ, UK
[c] Physics Department, Faculty of Science, Mansoura University, Mansoura 35516, Egypt

ARTICLE INFO

Keywords:
A. Carbon fibers
A. 3-Dimensional reinforcement
B. Compression after impact
D. Acoustic emission

ABSTRACT

This study is devoted to the damage characterization of Non-Crimp Fabric (NCF), 2D plain-woven (2D-PW) and 3D orthogonal plain-woven (ORT-PW) carbon/epoxy laminates, subjected to compression after multiple-impact loading, using Acoustic Emission (AE). The ultrasonic C-scan images showed that the interlaminar damage area induced by the single and 3-impact in ORT-PW architecture is 3 and 2 times smaller than NCF and 2D-PW architectures respectively. The impacted specimens were then subjected to the in-plane compression load. Two indices, one based on the mechanical response and another one based on the AE behavior of the laminates, were proposed to compare the performance of different architectures. These indices showed that the ORT-PW had the best performance among all the architectures. Finally, AE was used to distinguish the different damage mechanisms including: matrix cracking, intra and inter-yarn debonding, defected-fiber breakage, intact-fiber breakage and z-binder fiber breakage in the CAI tests of the architectures.

1. Introduction

Fiber-reinforced composites have been extensively used in aerospace, automotive and wind energy industries thanks to their high strength and stiffness to weight ratio compared to traditional metals. Nowadays, the most popular type of composites, used in industrial applications, are in the form of two-dimensional (2D) composites, made of unidirectional or woven plies. They are characterized by high in-plane properties while their out-of-plane properties are relatively poor. This makes them susceptible to severe damage when subjected to low velocity/low energy impact loading. Three-dimensional (3D) woven composites have been introduced as an alternative to enhance the out-of-plane properties of composite materials [1]. However, low velocity impact (LVI) still represents a serious threat to their use in real life applications as they can cause barely-visible impact damage (BVID) which can go undetected. Thus, several studies investigated the impact resistance of unidirectional (UD) [2], non-crimp fabric (NCF) [3], 2D [4,5] and 3D [4–7] woven composites subjected to LVI. In addition, damage tolerance, defined as the ability to maintain the undamaged or initial strength at the presence of damage, was quantified by measuring the residual strength after impact in tension (TAI), compression (CAI) and flexure (FAI). Having a reliable real-time damage detection technique is important for monitoring the structural integrity of 2D laminated and 3D woven composites, especially when it comes to the non-visible damage that may lead to catastrophic failure. Structural health monitoring (SHM) techniques, such as: optical fibers [8], acoustic emission (AE) [9,10], lamb waves [11,12], electromagnetic sensors [13] and electrical resistance monitoring [14], have been widely used for damage detection in composites.

Among aforementioned SHM techniques, AE has demonstrated a good performance for damage assessment in laminated composites. This technique has been widely used for damage characterization in NCF and 2D woven architectures under different loading conditions such as interlaminar fracture modes: I [15–18], II [19–21] and mixed-mode I&II [22,23], tensile [24,25], compressive [26], out-of-plane indentation [27,28], LVI [29–31] and CAI [32]. However, in the case of 3D woven composites, the available literature has been mostly concentrated on the AE-based damage evaluation in these materials under tensile loading condition. For example, Li et al. [33] clustered the damage mechanisms in 2D and 3D woven carbon/epoxy laminates under tensile loading using AE. The principal component analysis showed that the peak amplitude and frequency are the best features to discriminate

* Corresponding author.
E-mail address: m.saeedifar@tudelft.nl (M. Saeedifar).
[1] Co-first author.

https://doi.org/10.1016/j.compositesa.2020.105833
Received 7 December 2019; Received in revised form 6 February 2020; Accepted 13 February 2020
Available online 14 February 2020

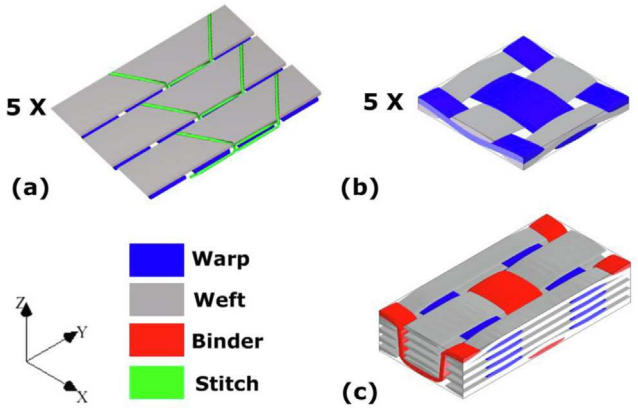

Fig. 1. Schematic of the different types of investigated composites: a) NCF, b) 2D-PW and c) ORT-PW (the warp yarns highlighted in blue, the weft yarns in grey, the through thickness binders in red, and the stitch yarns for the NCF in green) [6]. (For interpretation of the references to color in this figure legend, the reader is referred to the web version of this article.)

AE signals. They reported that the high frequency AE signals were originated from the fiber bundle breakage. The same authors [34] used AE to differentiate four damage mechanisms including matrix cracking, fiber/matrix debonding, delamination and fiber breakages in 2D and 3D glass/epoxy laminates under tension loading. They used the waveform shape, amplitude and frequency features to identify the different damage modes. The results showed that matrix cracking was identified with low amplitude, medium rise time and medium duration; while interface debonding was characterized with short rise time and short duration. Furthermore, delamination signal was represented by medium amplitude, medium rise time and long duration. In a similar manner, Lomov et al. [35] investigated the sequence of damage modes in tension. They reported that the damage initiated in the form of matrix cracks normal to the loading direction located around the yarns. This was then followed by the formation of longitudinal cracks parallel to the loading direction, at the interface of yarns and matrix. The last activated damage mechanism was cracks formation at the interface of z-yarns and matrix. To resemble a more complicated but realistic case, Tableau et al. [36] detected the damage initiation in 3D woven carbon/epoxy specimens under multi-axial incremental tension loadings using AE. The AE results were consistent with macroscopic shear rigidity loss and in-situ video microscopy observations.

Based on the available literature, no work has been done on the assessment of LVI and CAI-induced damages in 3D woven composites using AE. Moreover, from the application point of view, the composite structure are susceptible to repeated impacts at different locations, which, according to the authors' knowledge, has not been comprehensively investigated in literature. Therefore, the main novelty of the present study is: using AE for damage assessment in 3D woven

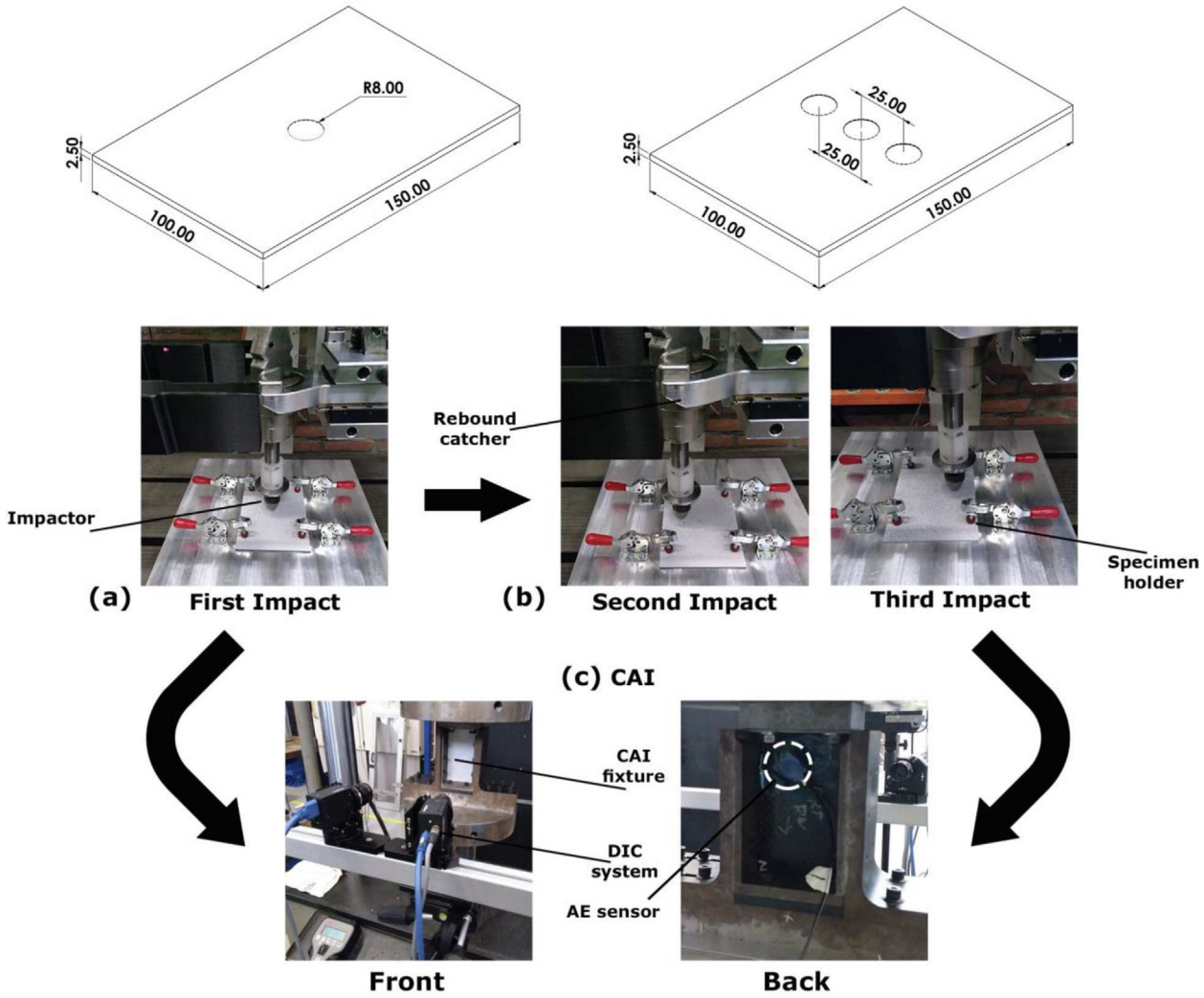

Fig. 2. Testing setup: a) first impact, b) second and third impacts and c) CAI.

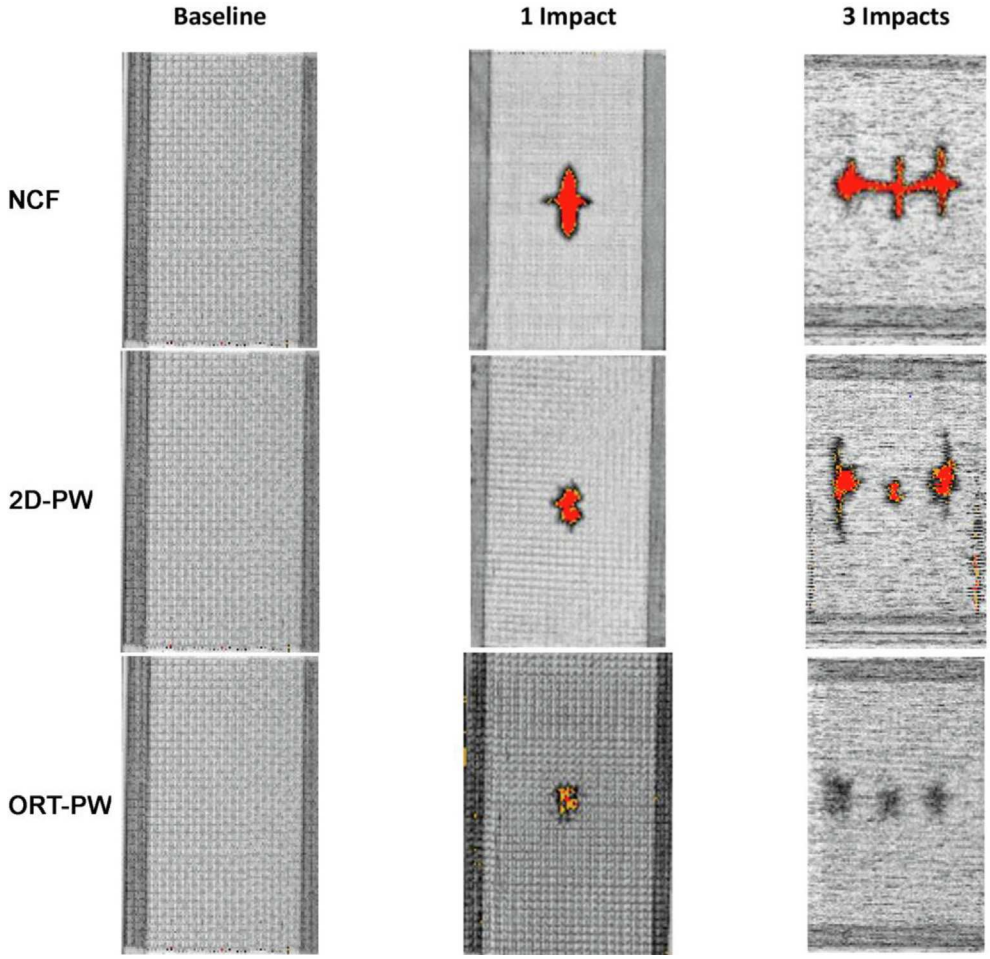

Fig. 3. Ultrasonic C-scan images of different architectures before and after single and multiple LVI test.

Table 1
The percentage (%) of impacted area for single and repeated impact cases.

	Single Impact	Three Impacts
NCF	1.81 ± 0.29	4.01 ± 0.11
2D-PW	1.05 ± 0.12	2.35 ± 0.16
ORT-PW	0.66 ± 0.08	1.43 ± 0.27

composites subjected to compression after multi-impact (CAMI) loading, and then comparing the damage behavior, detected by AE, with NCF and 2D woven architectures. With the aid of Digital Image Correlation (DIC), X-ray Computed Tomography (X-ray CT) and Scanning Electron Microsopy (SEM), the AE results were verified and interpretted. Previous researchers [37–40] clearly reported the advantage of combining such techniques in damage characterization of composite materials. It is worth mentioning here that the mechanical characterization of the effect of multiple impacts on the damage resistance and damage tolerance of these architectures has been recently published in detail by the authors in [6].

2. Materials and manufacturing

The three architectures of interest in this study are non-crimp fabric (NCF), 2D plain-woven (2D-PW) and 3D orthogonal plain-woven (ORT-PW). The ORT-PW consists of 5 warp and 5 weft layers, including the z-binding yarns in the warp. In the case of NCF and 2D-PW, five layers are used so that all the produced fabrics have approximately the same areal density (~2000 g/m^2). The unit-cell for these architectures is depicted

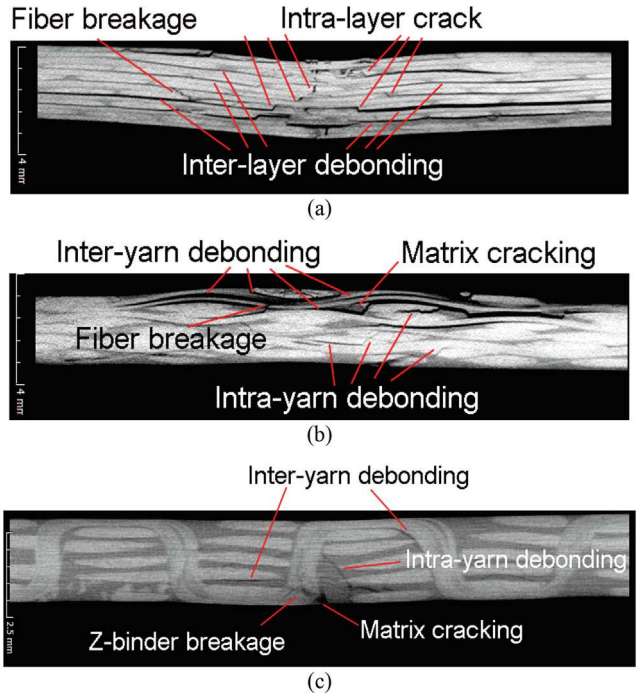

Fig. 4. 3D X-ray CT image of a) NCF, b) 2D-PW and c) ORT-PW architectures after single LVI.

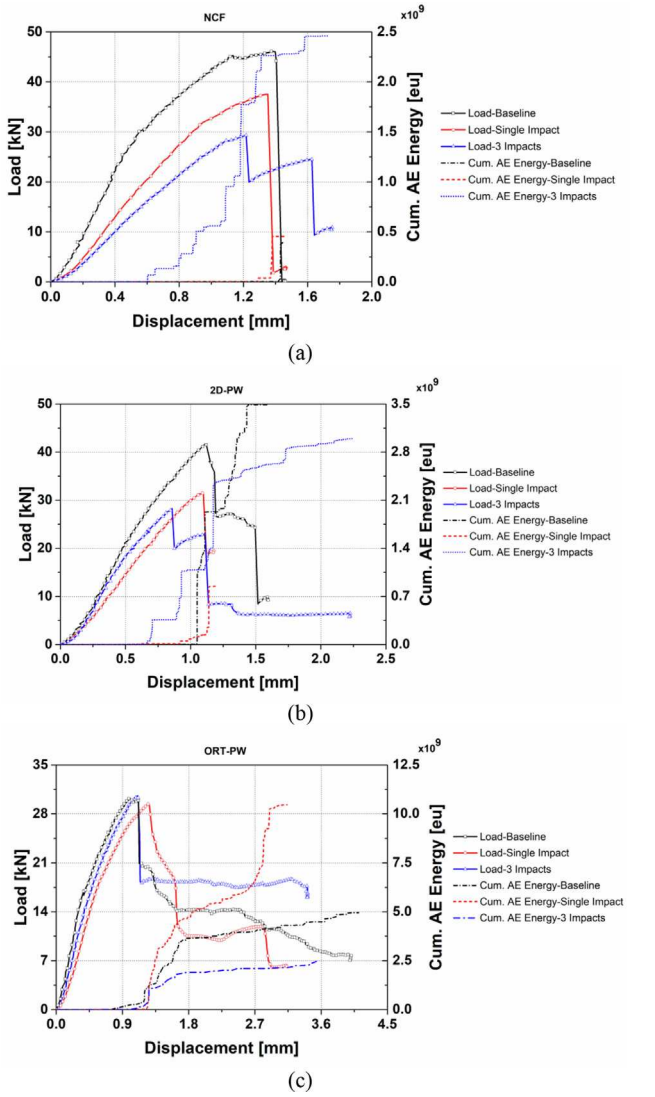

Fig. 5. The load and cumulative AE energy versus displacement curves for the CAI tests of a) NCF, b) 2D-PW and c) ORT-PW specimens.

in Fig. 1. The unit-cell is defined as the smallest volume element that can represent the composite constituents, geometrical features and yield homogenized properties representative for the whole structure. The carbon fiber used is T700-12 k; while the resin system is Gurit T-Prime 130–1 having a mixing ratio of 100/27 by wt% of resin/hardener. A resin transfer molding (RTM) tool of 500 mm × 500 mm, manufactured by Composite Integration Ltd., was used to infuse the composite panels, with a thickness of ~ 2.5 mm and fiber volume fraction of ~ 50%. The curing cycle recommended by the manufacturer was used as detailed in [41].

3. Experiments and characterization

3.1. Impact testing

Impact testing for all specimens was conducted using a drop-weight tower according to ASTM D7136 [42]. To ensure that the impactor strikes the specimens only once, the impact tower was equipped with a rebound catcher (see Fig. 2). Based on the ASTM standard, the support fixture has a cut-out of 125 ± 1 mm in the length direction and 75 ± 1 mm in the width direction. As the scope of this study is the LVI, impact energy was set to 15 J using a hemi-spherical impactor with a diameter of 16 mm and a mass of 4 kg, as depicted in Fig. 2. For the first set of specimens, they were all impacted in the center; while the second set of specimens were impacted two more times (left and right), 25 mm apart from the first impact (see Fig. 2) with the same impactor and impact energy. As the impactor diameter was 16 mm, the location of the 2nd and 3rd impacts were determined to avoid overlap of the individual impacts. Due to using the same support fixture, the boundary conditions for the 2nd and 3rd impacts were different from the 1st impact. The effect of the boundary conditions during impact testing has been reported in [6].

3.2. CAI testing

CAI testing for all specimens was conducted according to the ASTM D7137 [43]. The test set up is shown in Fig. 2c. For baseline comparison, non-impacted specimens from each architecture were tested in compression using the same test setup. For the impacted specimens as previously highlighted, there were two sets of CAI testing. The single-impacted specimens (see Fig. 2a) were directly tested in compression after the first single impact (see Fig. 2c). However, the multiple-impacted specimens were tested in compression after going through the process of three impacts as depicted in Fig. 2b&c. All specimens were loaded in compression, in a displacement-controlled mode, with a crosshead displacement of 1.25 mm/min. The crosshead displacement and the applied force were recorded using a 500 kN load-cell MTS 810 hydraulic testing machine. Digital Image Correlation (DIC) was used on the front side of the specimen while the AE sensor was placed on the back side as shown in Fig. 2c.

3.3. Ultrasonic C-scanning

Ultrasonic C-scanning was used as a non-destructive testing (NDT)

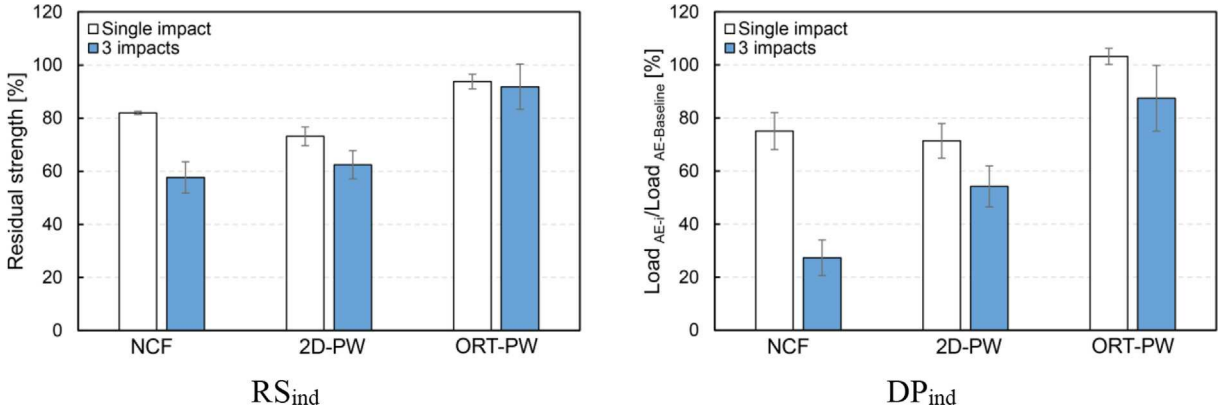

Fig. 6. The residual strength index (RS_{ind}) and damage propagation index (DP_{ind}) for different architectures.

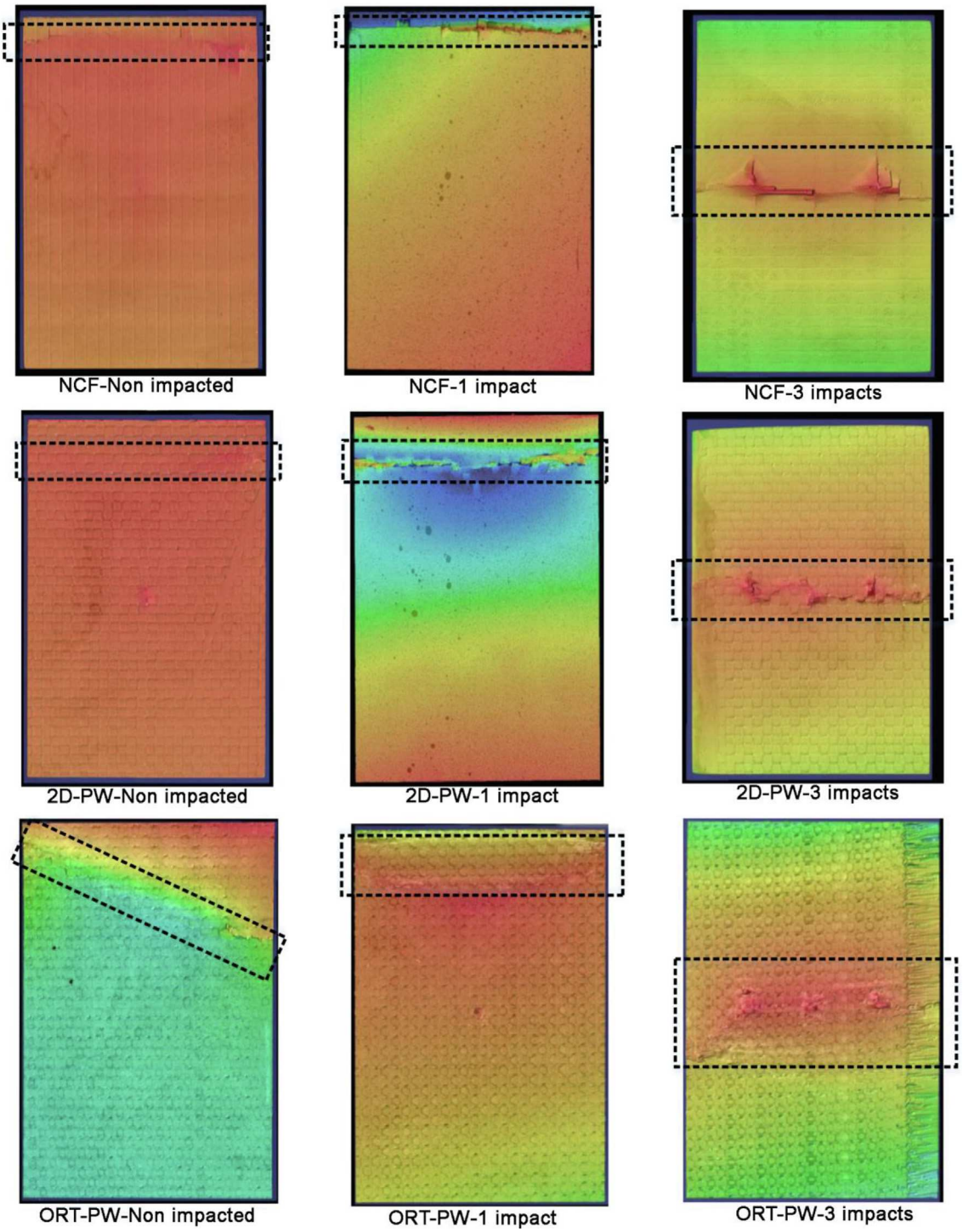

Fig. 7. The 3D surface scanning of different architecture after CAI tests (the collapse region is shown by a black rectangular).

technique to quantify the level of induced damage due to impact and CAI of the different architectures. A Midas NDT system, having 10 MHz transmitter and receiver transducers, was used. With Zeus software, the scanning speed was set to 200 mm/min.

3.4. X-ray Computed Tomography (CT)

To reveal the internal damage due to impact, X-ray CT scans were performed for the different types of impacted specimens using a Nikon XTH-320 machine. The 225 kV source with reflective target was used with a 0.125 mm copper filter. The total volume in the field of view was 22.5 × 19 × 5.5 mm3, with a resolution of ~ 13.2 μm. The source current and voltage were set to 59 μA and 220 kV respectively. With a total of 3142 radiographs being collected over 360° and ~ 1.4 s exposure time for each radiograph, the total data acquisition time was ~ 1.25 h. After scanning, the raw data was used to reconstruct the 3D volume using VGSTUDIO MAX software.

3.5. Acoustic emission

The AE events of specimens under CAI tests were recorded by one AE sensor placed on the back side of the specimen. The used AE sensor,

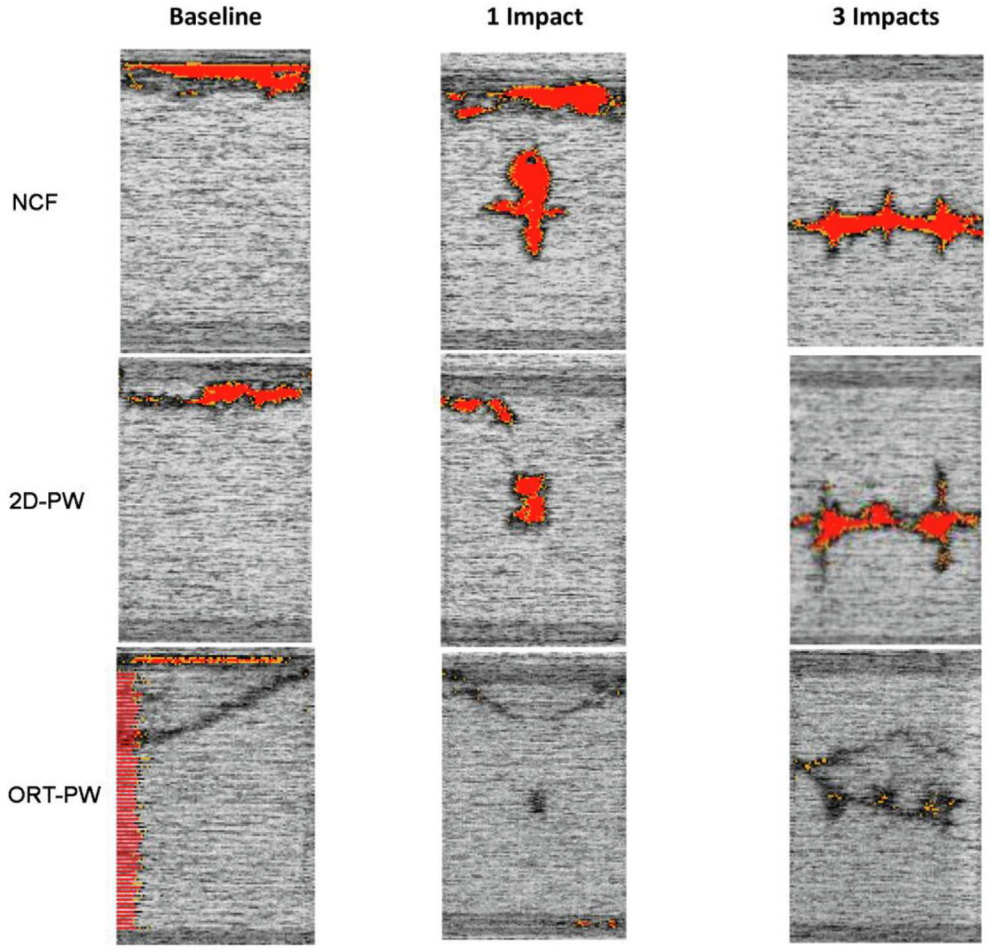

Fig. 8. Ultrasonic C-scan images of different architectures after CAI test.

Table 2
The percentage of damage area of different architecture after the CAI test.

Specimen	Baseline	Single Impact	Three Impacts
NCF	8.29	14.49	9.85
2D-PW	7.99	5.32	15.49
ORT-PW	6.03	3.51	7.67

AE1045SVS900 M, is a broadband single-crystal piezoelectric transducer with the operational frequency range of [100–900 kHz] supplied by Vallen Systeme GmbH. In addition, an external 34 dB pre-amplifier was used to amplify the recorded signals. In order to eliminate the signals originated from the friction between the CAI fixture's parts, the threshold was set to 50 dB. The AE data was collected with a sampling rate of 2 MHz by the AMSY-6 Vallen, 8-channel AE system. Ultrasound gel was applied to improve the coupling between the AE sensor and the specimen's surface. The performance of AE system was validated before each test by conducting a standard pencil lead break procedure [44].

3.6. Digital image correlation (DIC)

To capture the displacement contour map during the test, a three-dimensional (3D) DIC system (see Fig. 2c) was used. The system consisted of two 5 MP 8-bit "Point Grey" cameras with "XENOPLAN 1.4/23" lenses. The speckle pattern images were captured by ViC-Snap 8 software with an acquisition rate of 2 frames per second (fps). Afterwards, these images were processed using ViC-3D 8 software. The processing parameters were as follows: subset size of 100 × 100 pixels and step size (distance between subsets) of 7 pixels. The observation window was approximately (120 × 70) mm^2 which was equivalent to an image with dimensions of (2048 × 1194) pixels.

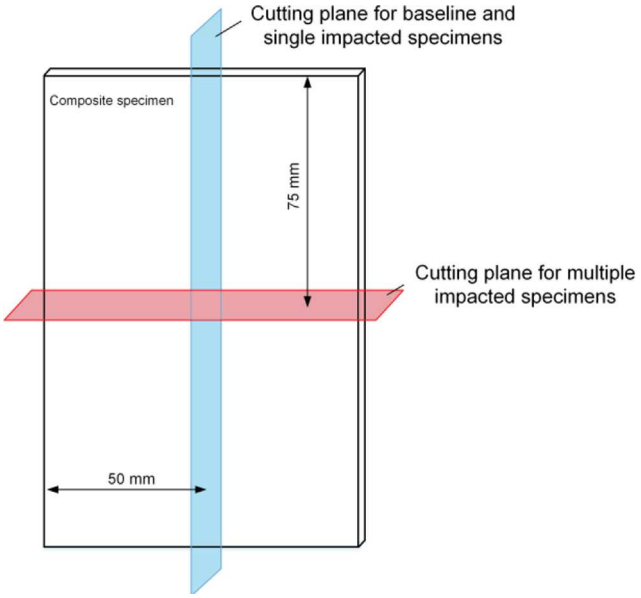

Fig. 9. Cutting planes for observing the cross section of the specimens.

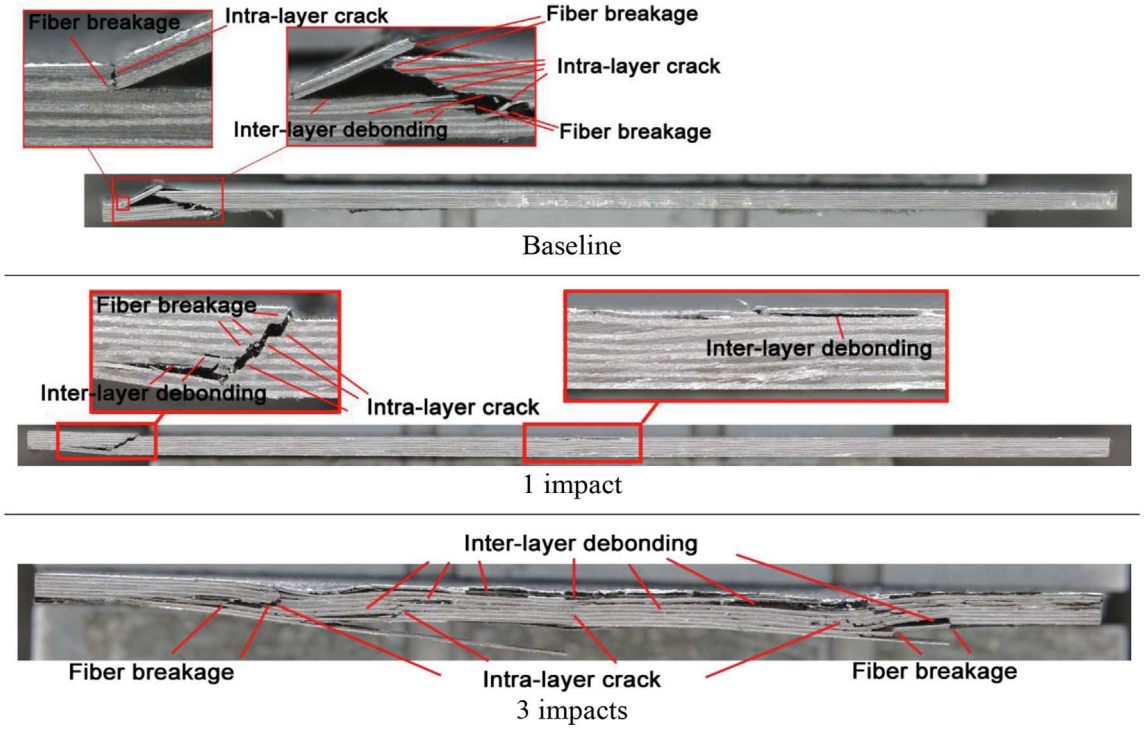

Fig. 10. Microscopy images of the cross section of NCF specimen after CAI test.

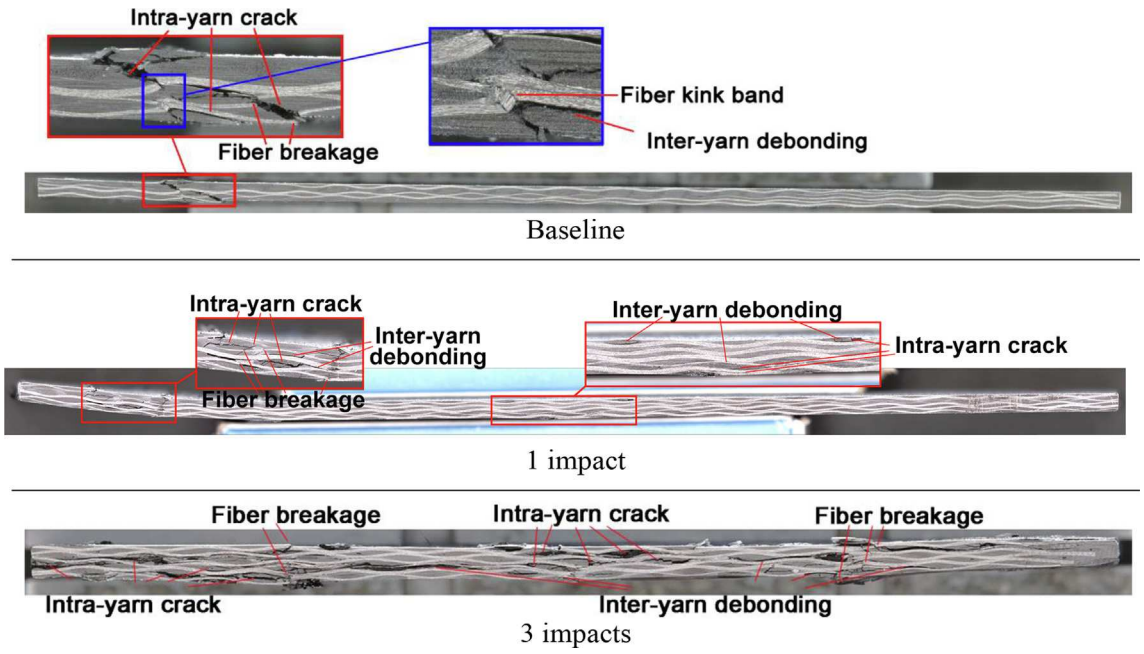

Fig. 11. Microscopy images of the cross section of 2D-PW specimen after CAI test.

4. Results and discussion

4.1. Single and multiple impacts

The specimens were subjected to single and three impacts as detailed in section 3.1. Ultrasonic C-scan and 3D X-ray CT were used to assess the interlaminar and intralaminar damages induced by LVI in the specimens. The ultrasonic C-scan images of the non-impacted and impacted specimens, before CAI tests, are shown in Fig. 3. The percentage (%) of damaged area for different architectures were calculated using the image segmentation tool available in MATLAB software and they are reported in Table 1. The percentage of damaged area for ORT-PW architecture is 3 and 2 times smaller than NCF and 2D-PW architectures respectively. This is due to the presence of binders in the ORT-PW architecture which arrest interlaminar damage. As shown in the X-ray CT images (see Fig. 4), the through-thickness binding yarns of ORT-PW specimen suppressed the interlaminar damage from propagation along the plies' interface, and it finally resulted in the reduction of the damage area in the 3D woven architecture.

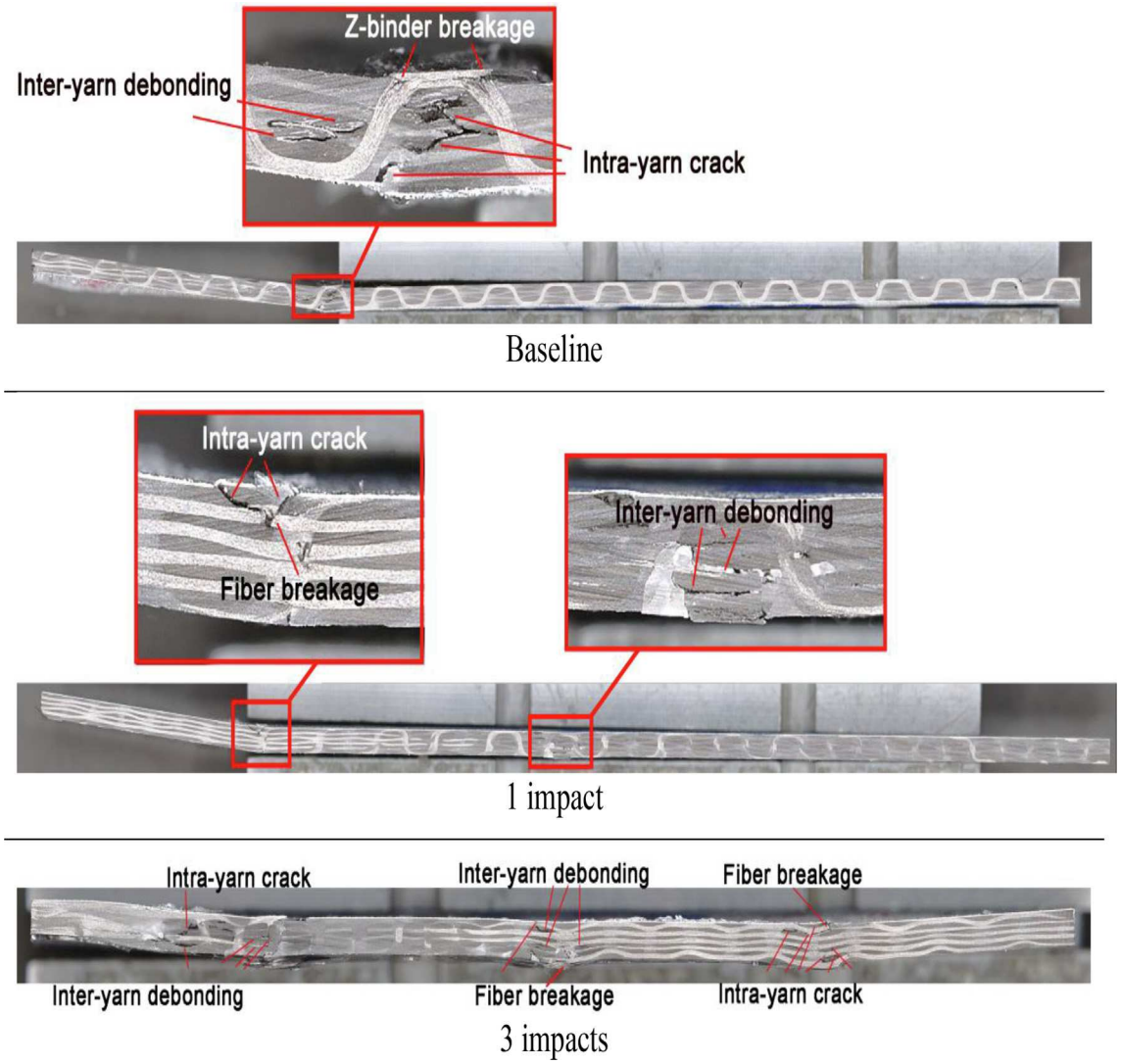

Fig. 12. Microscopy images of the cross section of ORT-PW specimen after CAI test.

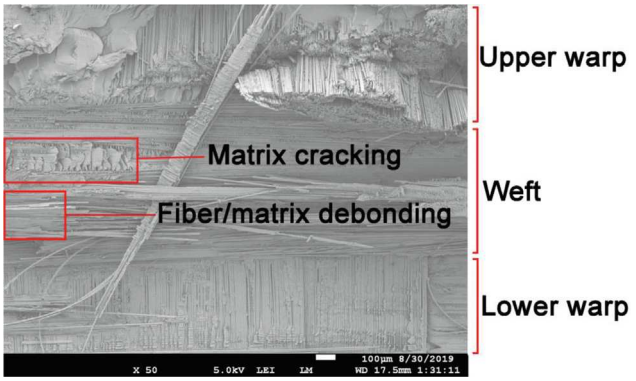

Fig. 13. The scanning electron microscopy image of intra-yarn crack in 2D-PW architecture.

4.2. CAI results

The load and cumulative AE energy versus displacement curves of the CAI tests are depicted in Fig. 5. The AE energy was calculated as the the area under the waveform squared within the waveform's duration. By comparing the load–displacement curves for different architectures, it is clear that the stiffness and maximum strength of the NCF specimen are significantly affected by the single and multiple impacts; while the mechanical behavior of ORT-PW specimen shows the minimum dependency on LVIs. To accurately quantify the mechanical performance of the different architectures, two indices are defined as follows: CAI's residual strength, which is defined as the ratio of the maximum load of the impacted specimen to the maximum load of the non-impacted specimen for the same architecture during CAI. The second index focuses on the detection of damage growth using AE. So, if the first significant jump/increase in the cumulative AE energy is considered as the moment that the damage starts to propagate, its corresponding load can be considered as the AE critical load. The ratio of this load for the impacted specimen to the non-impacted specimen is defined as the damage propagation index. As all the specimens have the same nominal thickness, there is no need to normalize the indecies in the form of stresses as the ratios/trend should be the same. The residual strength index (RS_{ind}) and damage propagation index (DP_{ind}) for different architectures are depicted in Fig. 6. RS_{ind} shows that the NCF architecture has the largest reduction in the residual strength due to single and multiple impacts (~20% and 45% respectively). In the case of 2D-PW, the residual strength reduction caused by single and multiple impacts is still considerable (~25% and 35% respectively). While, this index does not show any significant reduction in the residual strength of ORT-PW architecture due to LVIs. In Consistent with RS_{ind}, DP_{ind} reveals that the AE critical load (load corresponded to the damage propagation) of the

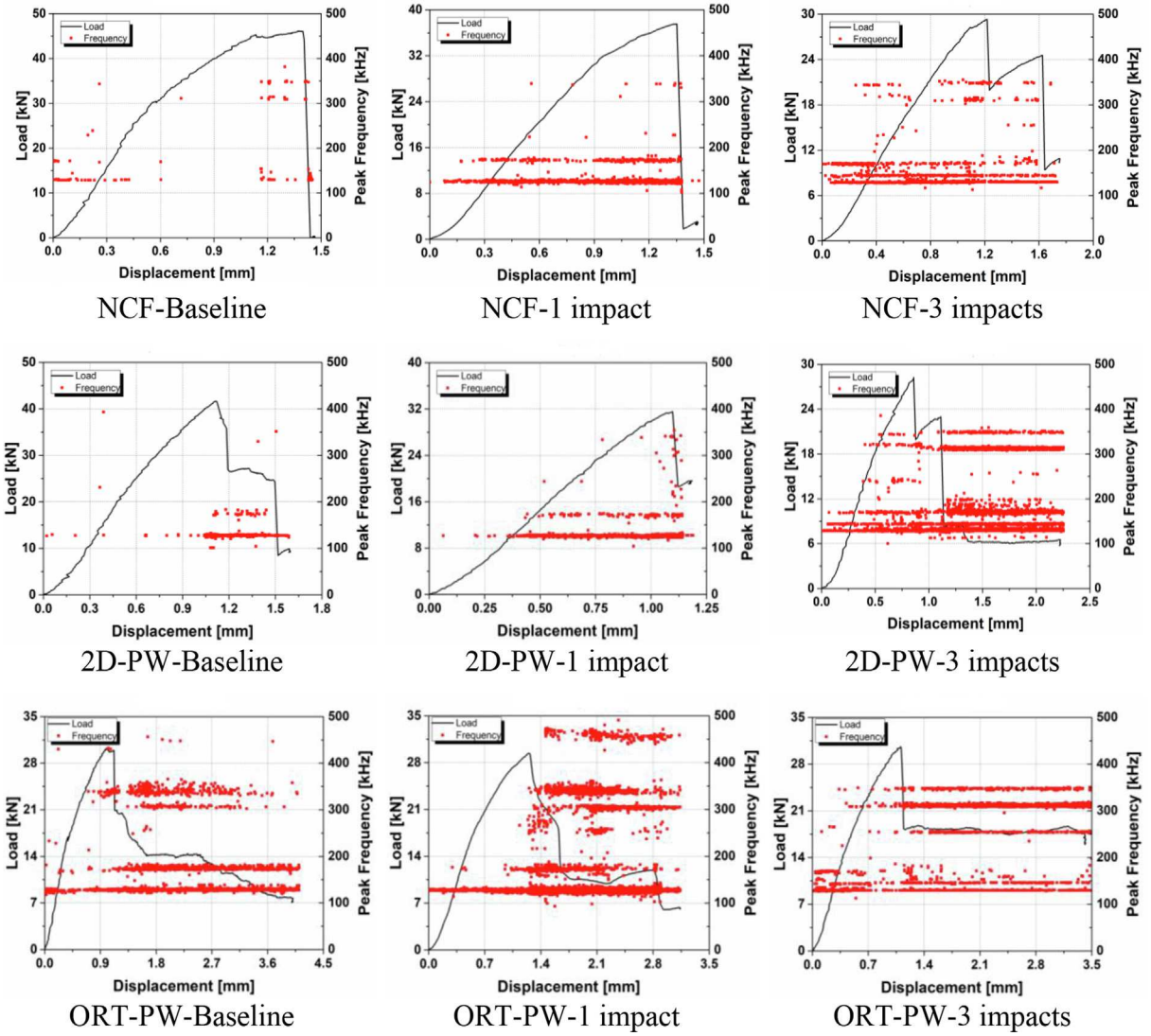

Fig. 14. The peak frequency distribution for different architectures during CAI tests.

NCF architecture decreased 20% and 70% after the single and multiple impacts, and the AE critical load reduction for 2D-PW is around 40%. On the contrary, DP_{ind} does not show any significant reduction in the AE critical load for the ORT-PW architecture. Therefore, both indices demonstrate the better performance of ORT-PW in comparison to NCF and 2D-PW architectures.

The failure mode of different architectures under CAI loading is shown in Fig. 7. In order to highlight the region at which final failure occurred, the surface of the specimens was scanned by a 3D surface scanner. As per the ASTM D7137 standard [43], the designated failure code for the non and single impacted cases is LGM where L stands for lateral failure; G is gauge/away from damage failure area, and M is the middle location. This fact reveals that the damage induced by the single impact was not severe enough to affect the global behavior of the laminates under CAI [6]. On the other hand, all the 3-impacted specimens were broken at the middle of the specimens where they had been already impacted. The three-letter failure code for this case is LDM; where D corresponds to at/through damage failure area. Thus, the multiple LVI-induced damage was severe enough to weaken the specimen at the impact region leading to the final failure at the middle of the specimen.

The ultrasonic C-scan images of the specimens after the CAI are depicted in Fig. 8. In the case of the non-impacted specimens, there is no significant difference of the damaged area among the three architectures. This can be attributed to the fact that they all failed at the unsupported gauge length due to buckling. However, once these specimens were impacted, the difference captured by the C-scan is clear. According to the percentage of the damaged area reported in Table 2, in the case of single impact, the damage area of ORT-PW architecture is 4 and 1.5 times smaller than NCF and 2D-PW architectures respectively, and in the case of multiple-impact, it is 1.3 and 2 times smaller than NCF and 2D-PW architectures respectively.

To comprehensively study the damages in the specimens, they were cut by a CNC cutting machine instrumented by a sharp rotary cutting blade, and their cross section was observed by the microscopy images. In order to show the impact-induced damage and the CAI-induced damage at the same section, for 3-impacted specimens, which the final failure occurred at the impacted region, they were cut in the middle of specimen perpendicular to the loading direction. While, for the other ones, which failed near the top edge of the specimen, to show the impact-induced damage at the middle and the CAI-induced damage at the top region, they were cut along the specimen's length as clarified in Fig. 9. As shown in Fig. 10, the main damage mechanisms for the non-impacted and single-impacted NCF specimens were intra-layer crack, inter-layer debonding and fiber breakage. The damage mechanisms of the non-impacted and single-impacted 2D-PW specimens were the same; with the difference that the inter-yarn debonding is guided by the waviness along the warp direction (see Fig. 11). According to Fig. 12,

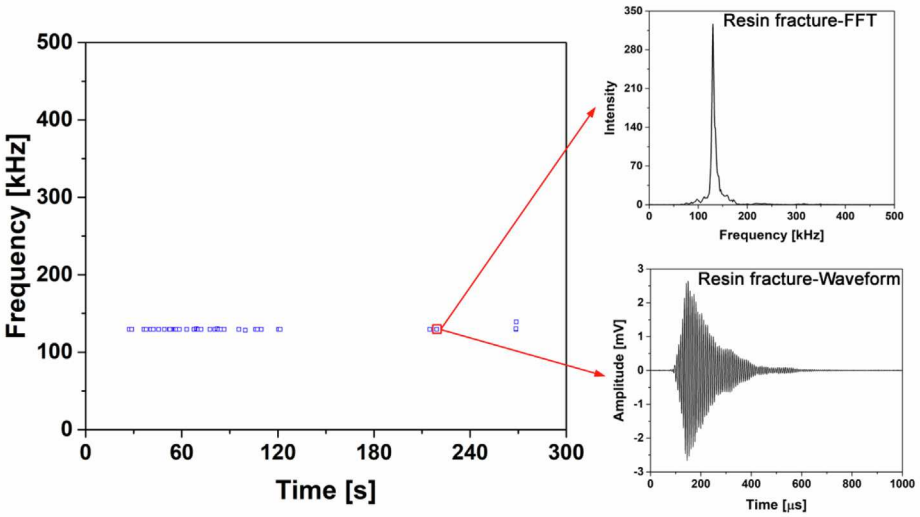

(a)

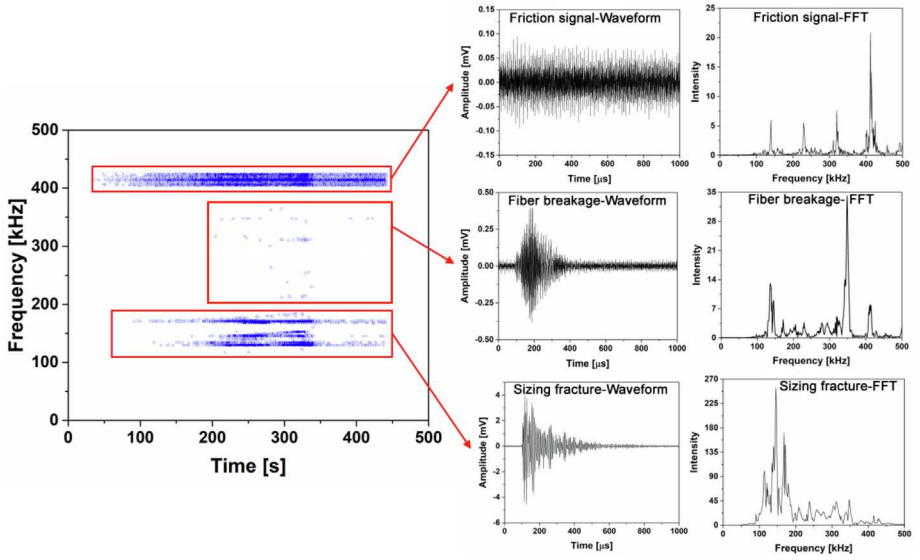

(b)

Fig. 15. The frequency distribution of a) resin and b) carbon fiber bundle fracture.

the inter-yarn debonding in the non-impacted and single-impacted ORT-PW specimens is suppressed by the z-binding yarns and it is constrained to one unit cell. Also, some binder breakages are captured at the compression side of this specimen. In the case of multiple-impacted specimens, severe damages occurred in the NCF and 2D-PW specimens, across the width of specimen, while the damage of ORT-PW architecture is mostly localized around the impacted zones. The intra-layer/yarn crack could be further divided into two forms: matrix cracking and fiber/matrix debonding (intra-layer debonding) as shown in Fig. 13 for 2D-PW architecture, just as a representative case.

Each damage mechanism in laminated composites usually generates AE signals with almost unique AE features [28,45]. Among all the AE features, like amplitude, rise time, duration, energy, centroid frequency and peak frequency, two features have been extensively used in literature for distinguishing damage mechanisms: peak frequency and amplitude. As peak frequency is not highly affected by the attenuation phenomenon, it represents a better damage identification parameter in comparison with the amplitude. The peak frequency distribution of the AE signals recorded during the CAI tests for different architectures is shown in Fig. 14. Generally, five AE clusters can be distinguished for NCF and 2D-PW architectures, including [100–150 kHz], [150–200 kHz], [200–300 kHz], [300–325 kHz] and [325–400 kHz]. In the case of ORT-PW, besides the aforementioned clusters, there is another cluster with the frequency of [400–500 kHz]. These different clusters may be related to the different damage mechanisms occurred in the specimens.

In order to correlate the AE clusters to different damage mechanisms, the AE features of each damage mode should be identified individually. As already shown in Figs. 10 to 12, the main damage modes in the different architectures were matrix cracking, inter and intra-yarn debonding and fiber breakage. Accordingly, several tests were designed and performed to obtain the AE features of these damages. The AE features of fiber breakage were obtained by performing a tensile test on a bundle of T700-12 k carbon fiber tows. The AE signals of the fibers fracture were captured by the AE sensor mounted on the bundle's surface by a small plastic clamp. In addition, an ultrasonic gel was applied between the sensor and the yarn's surface to ensure a sufficient coupling quality. To obtain the AE features of matrix cracking, a

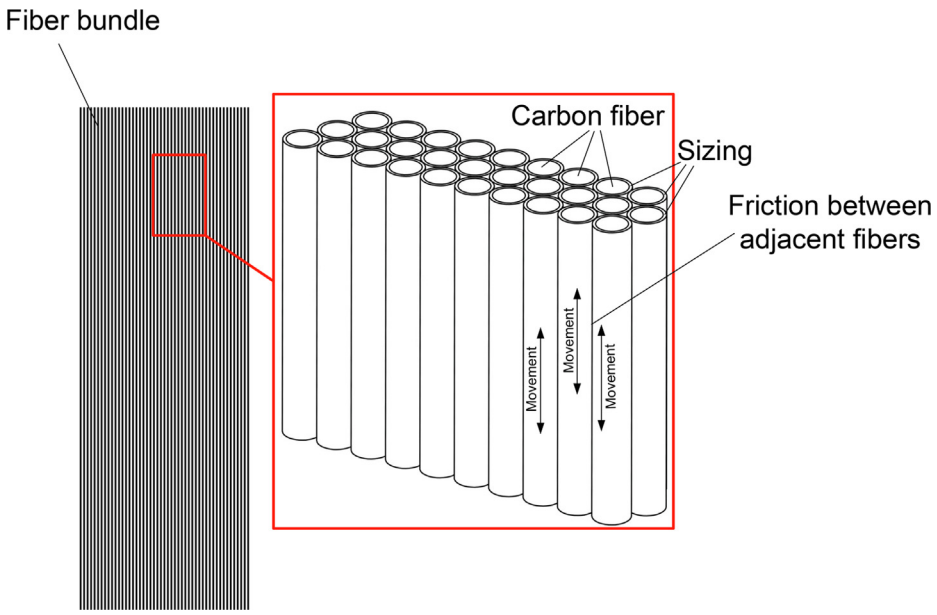

Fig. 16. The structure of carbon fiber bundle.

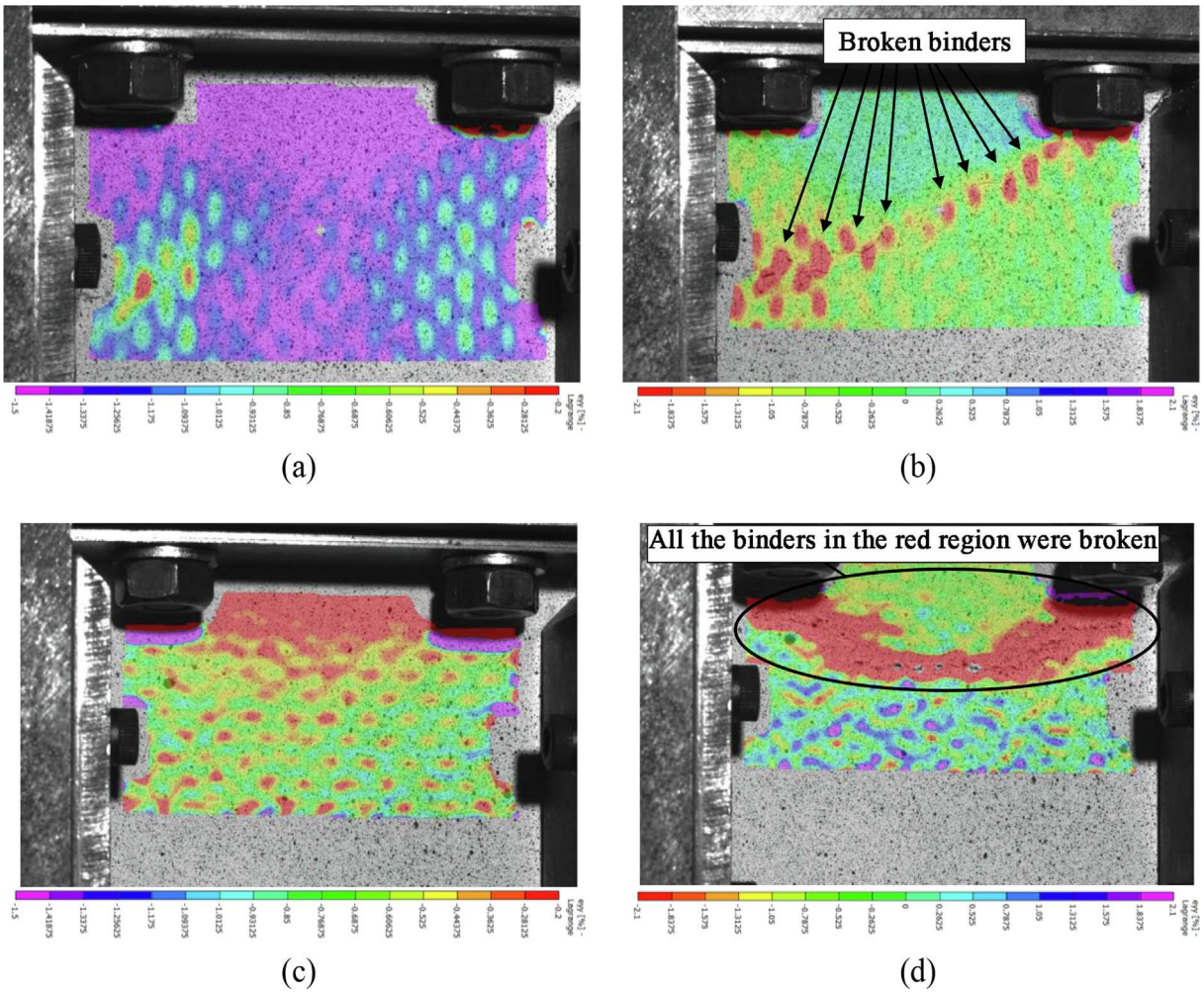

Fig. 17. The eyy strain (in the loading direction) distribution in ORT-PW architecture for a) the linear elastic segment of the load–displacement curve where no damage exists (z-binding yarns are visible), b) the final failure of baseline specimen, c) the linear elastic segment of the load–displacement curve where no damage exists (z-binding yarns are visible) and d) the final failure of single-impact specimen.

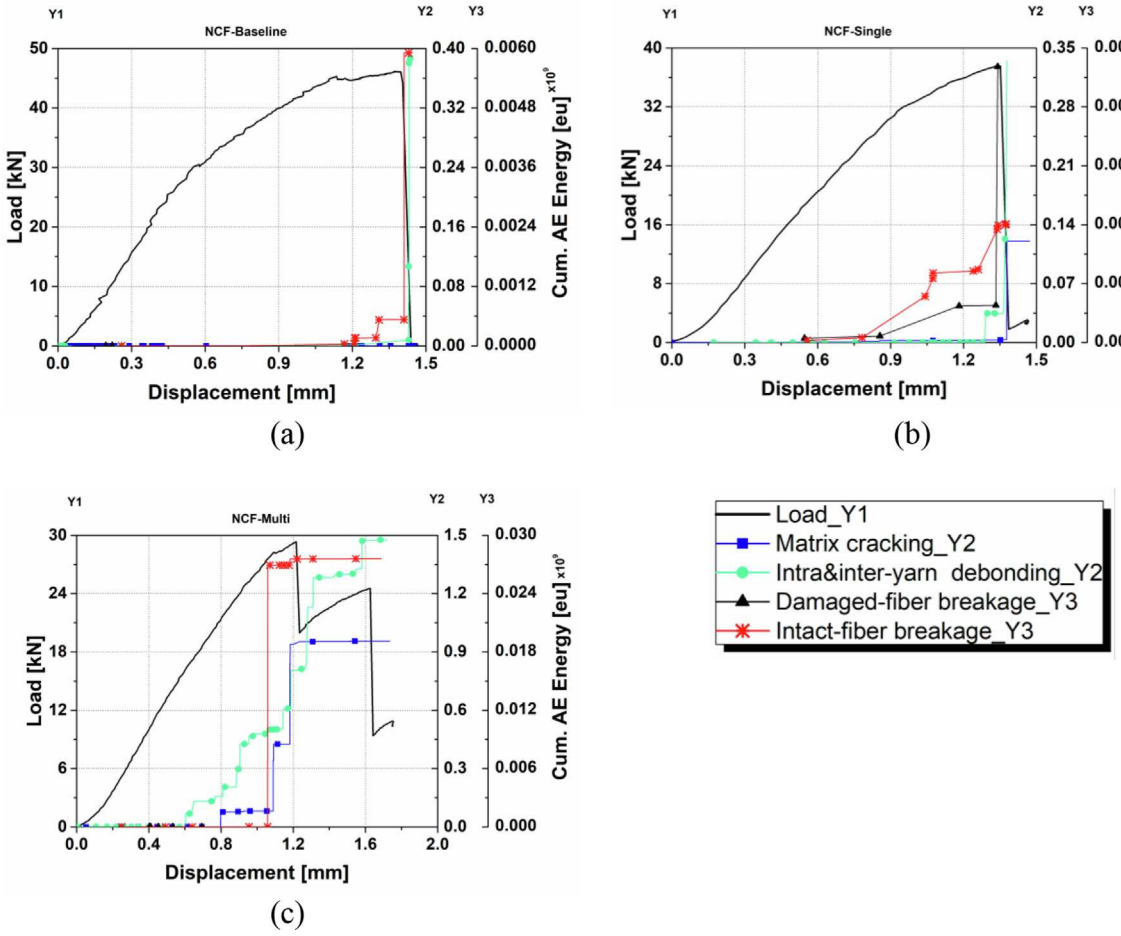

Fig. 18. The cumulative AE energy curve of different damage mechanisms for a) baseline, b) single-impact and c) 3-impact of NCF architecture.

rectangular strip was molded of the same epoxy resin used, and it was subjected to 4-point bending test. The AE signals originated from the fracture of the resin were captured by the AE sensor mounted on the resin specimen. The peak frequency distribution of the AE signals collected during fiber bundle and resin fracture tests are detailed in Fig. 15. According to Fig. 15a, the resin fracture induces signals with the frequency range of [100–150 kHz]. In the case of fiber bundle test (see Fig. 15b), there are four groups of AE events: the cluster with the highest frequency [400–500 kHz], two clusters with the frequency range of [200–300 kHz] and [300–370 kHz], and the cluster with the lowest frequency [100–200 kHz]. To find the origin of these AE clusters, the structure of the fiber bundle should be explained here. For illustration purpose, it is acceptable to assume that the fibers are perfectly aligned in the fiber bundle as shown in Fig. 16. To protect the fibers from fragmentation, filamentation and to reduce the friction between the fibers, especially during the weaving process, fibers are normally protected by a thin layer of a resin-compatible polymer, which is typically referred to as sizing. From AE point of view, by applying the load on the fiber bundle it is expected that the friction between the adjacent fibers generates some continuous signals from the early stages of the test. These friction signals are usually characterized by continuous waveforms, while the damage signals usually generate burst type waveforms. Then, by increasing the load, the sizing of the fibers starts to get damaged at the low load levels and finally carbon fibers will be broken at the high-load levels. A similar sequence of damages has been already reported for the tensile test of the uncured carbon prepregs [46], which is almost similar to the utilized fiber bundle in the present study. Therefore, the cluster with the highest frequency, shown in Fig. 15b, which produced continuous waveform is allocated to the friction between the fibers. The cluster with the least frequency, which was started at the low load levels, is due to sizing fracture. The two remained clusters can be assigned to the carbon fiber breakage, in a way that a few fibers that were partially defected/damaged during the fabrication and preparation process of the fiber bundle induce the low frequency signals [200–300 kHz], while the breakage of the rest intact fibers generates signals with the higher frequency, [300–370 kHz].

The results obtained from the resin and fiber bundle tests are used to assign the AE clusters of CAI specimens (see Fig. 14) to the different damage mechanisms. Accordingly, the AE signals with the frequency range of [300–400 kHz] are allocated to the breakage of the intact fibers due to CAI loading. As previously mentioned, the breakage of the partially damaged-fibers produces the AE signals with the lower frequency, [200–300 kHz]. Then the AE signals with this frequency range can be allocated to the breakage of the impacted-fibers during the CAI. Consistent with this fact, there are just a few AE events with this frequency range for CAI of baseline specimens that can be due to the breakage of a few fibers that have been defected during the manufacturing process. The number of AE signals with the frequency of [200–300 kHz] increases for single-impact specimens in which some fibers have been already damaged due to the impact. The number of these events for multiple-impact specimens is higher than the single-impact ones, which makes sense, because the number of damaged-fibers due to the multiple impacts is more than the single impact. Therefore, the AE signals with the frequency of [200–300 kHz], which are shown in Fig. 14, are dedicated to the damaged-fibers breakage.

Because the sizing layer always presents in-between carbon fiber and resin matrix in composite, it determines the fiber/matrix interfacial properties [47]. Therefore, the AE signals of the sizing fracture,

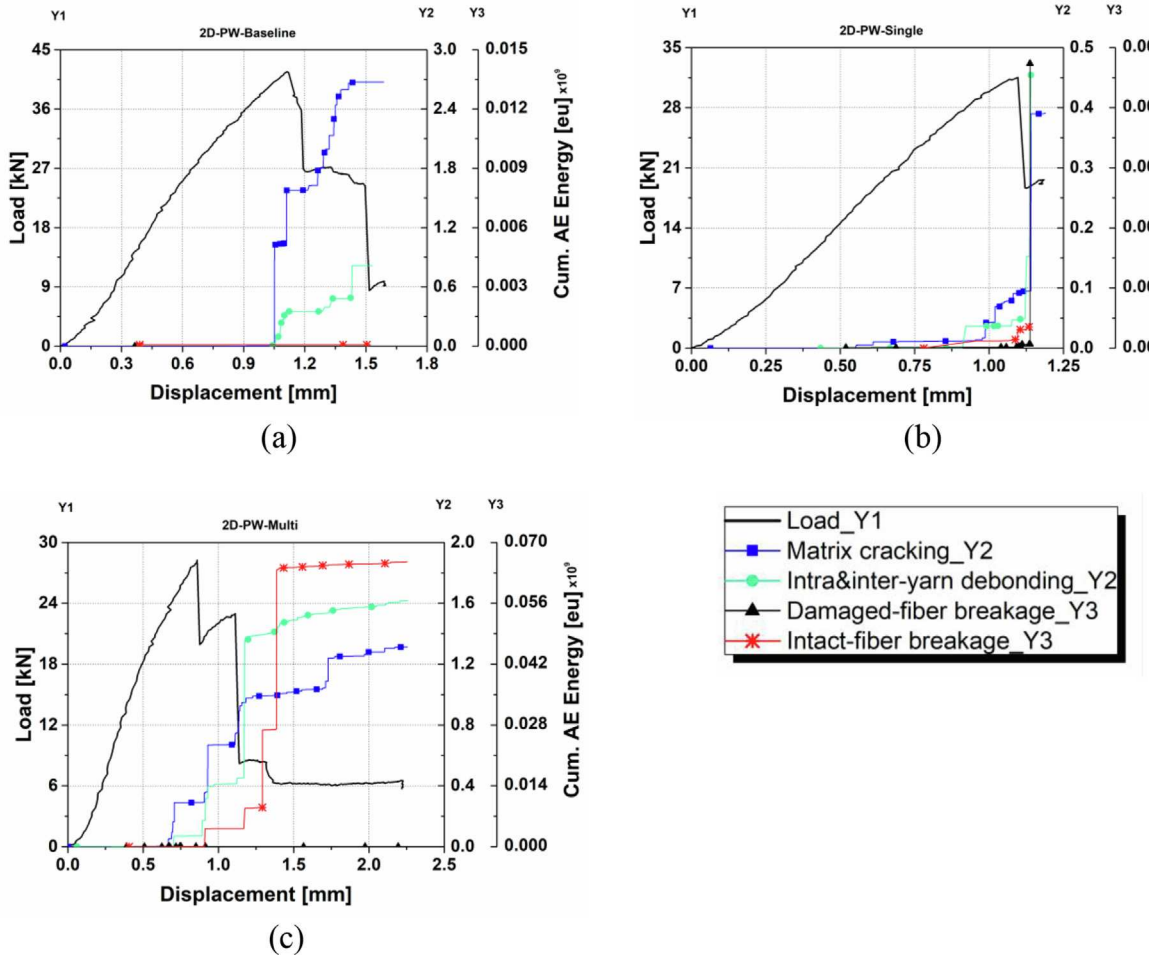

Fig. 19. The cumulative AE energy curve of different damage mechanisms for a) baseline, b) single-impact and c) 3-impact of 2D-PW architecture.

[100–200 kHz], correspond to the degradation of fiber/matrix interface, intra and inter-yarn debonding. However, as shown in Fig. 15, the frequency ranges of sizing failure and resin fracture are [100–200 kHz] and [100–150 kHz] respectively which have the common frequency of [100–150 kHz]. In other words, the signals with the frequency range of [100–150 kHz] can be related to either the matrix cracking or the debonding.

For appropriate partitioning of this cluster with the frequency of [100–150 kHz] into these two damage modes, a support vector machine (SVM) supervised classifier with a linear kernel was used. More information about this technique can be found in the reference [48]. First of all, seven frequently used features, including amplitude, rise time, duration, energy, counts, centroid frequency and peak frequency, were extracted for the whole AE signals of the resin fracture and the part of AE signals of the sizing fracture with the frequency of [100–150 kHz]. This data was then used to train the SVM classifier. When the SVM model was sufficiently trained (the accuracy of 96.9% obtained by the cross-validation method), it was employed to classify the group of AE signals of CAI tests with the frequency range of [100–150 kHz] into matrix cracking or debonding. The “resin fracture” labeled signals by the SVM were considered as the matrix cracking failure mode. Then, the “sizing fracture” labeled signals by the SVM were added to the AE signals with the frequency of [150–200 kHz] and assigned to the debonding failure mode in the CAI specimens.

In addition to the aforementioned damage mechanisms, there is a unique cluster of AE signals with the frequency of [400–500 kHz] for ORT-PW architecture, which does not exist in the other architectures (see Fig. 14). As the main difference of ORT-PW and the other two architectures is the presence of z-binding yarns, this AE cluster may be originated from their breakage. For the baseline and the single impact ORT-PW specimens, the final damage due to CAI test only happened in the top half of the specimen, in which the binders are still intact. This means there is some energy stored in them due to the pre-tension induced by the weaving process to produce such architecture. Once they break, they release this energy in a form of high-energy and high-frequency AE signals captured with the frequency of [400–500 kHz]. To confirm this interpretation, the average energies of the AE signals of the 2 clusters [300 to 400 kHz] and [400 to 500 kHz] were calculated. It was proven that the energy of the latter is almost twice the energy of the former. In the case of 3-impact ORT-PW specimen, the z-binding yarns were partially broken due to the impact loading, and the energy absorbed from the impact led to the release of the “pre-tension” of the binders. Thus, the AE signals of z-binding yarns breakage in 3-impact ORT-PW specimen due to CAI captured more or less with the same frequency of the signals obtained from the damaged-fiber breakage, i.e. [200–300 kHz]. Therefore, there is no cluster of [400 to 500 kHz] in 3-impact ORT-PW specimen. The last thing to confirm was the higher number of [400–500 kHz] AE events in the case of single impact vs the baseline. This was done using the DIC analysis which showed that the number of binders broken during the CAI test for the ORT-PW baseline was less than their counterparts in the single impact case (see Fig. 17(b and d)). The broken z-binders have been illustrated by red color corresponded to the failure strain of the carbon fiber, 2%.

After correlating the AE clusters to the different damage mechanisms, the evolution of each damage mechanism is investigated by plotting the cumulative AE energy curve of each AE cluster (see

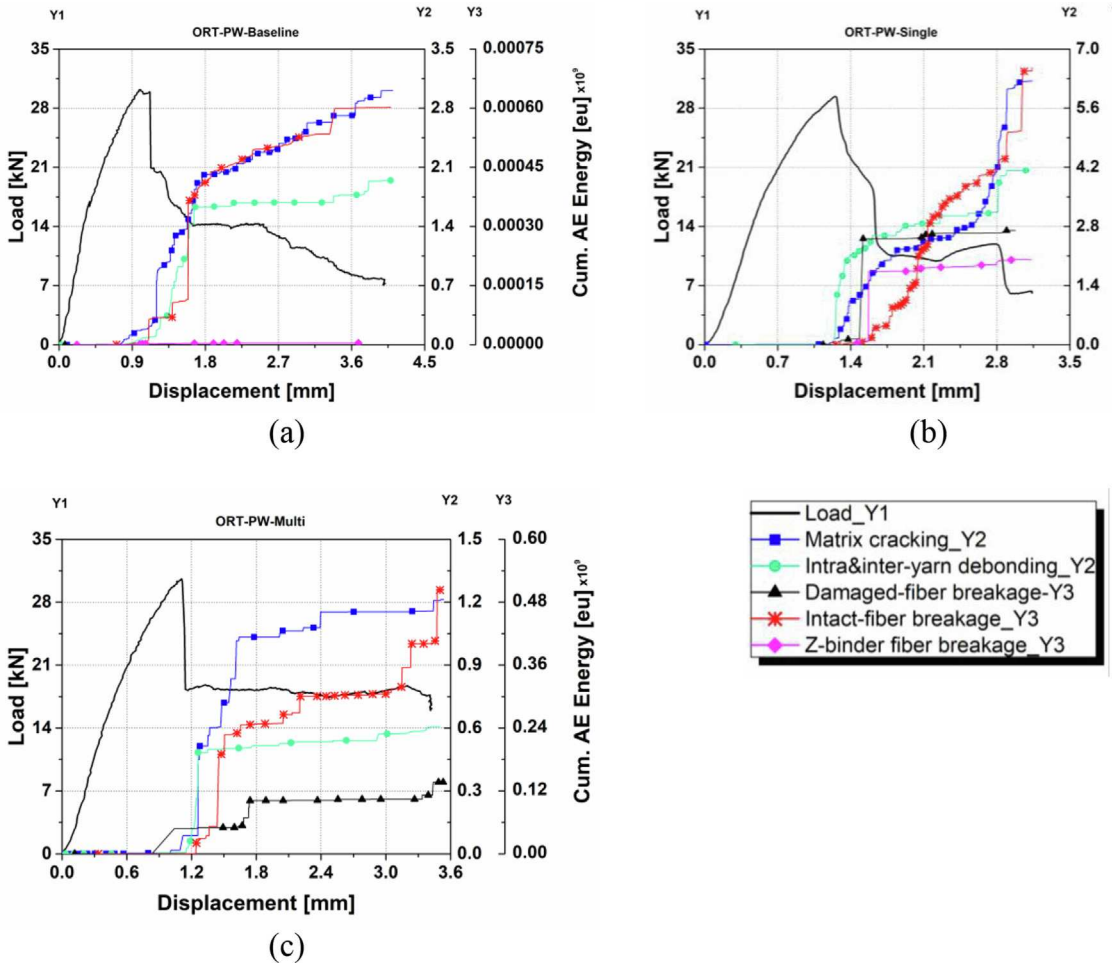

Fig. 20. The cumulative AE energy curve of different damage mechanisms for a) baseline, b) single-impact and c) 3-impact of ORT-PW architecture.

Figs. 18–20). For the NCF architecture, the dominant damage mode is debonding which makes sense, because there is no resistance against the propagation of the inter-layer debonding. While in the case of 2D-PW and ORT-PW architectures, due to the waviness of the warp and weft yarns and also the presence of z-binders, the required energy for the propagation of the inter-yarn debonding increases. Therefore, the dominant damage mode of 2D-PW and ORT-PW architectures changes to matrix cracking. Besides, in the case of NCF architecture, most of the damages occurred just before the maximum load, while for the 2D-PW and ORT-PW a progressive damage behavior is observed during the load-drop region after the maximum load.

5. Conclusion

The present study was devoted to the damage assessment of non-crimp fabric (NCF), 2D plain woven (2D-PW) and 3D orthogonal plain woven (ORT-PW) laminates subjected to compression after multiple-impact loading using AE. The key findings in this study can be summarized as follows:

1. The damage area induced by the single and 3 impacts, before CAI, for the ORT-PW architecture was 3 and 2 times smaller than NCF and 2D-PW architectures respectively.
2. The residual strength index, RS_{ind}, showed that ORT-PW architecture is the most damage tolerant among all the architectures. For the single-impacted case, RS_{ind} was ~1.2 times of NCF and 2D-PW, while for the 3-impacted case it was ~1.5 times of NCF and 2D-PW architectures.
3. Irrespective of the type of architectures, non-impacted and single impacted specimens failed due to buckling at the unsupported gauge length of the specimen. On the contrary, all the 3-impacted specimens were broken at the middle, where they were already impacted.
4. The fracture tests of the resin and fiber bundle revealed the following frequency ranges for the different damage mechanisms: matrix cracking [100–150 kHz], intra and inter-yarn debonding [100–200 kHz], the breakage of the impact-defected-fibers [200–300 kHz] and the breakage of the intact-fibers [300–400 kHz].
5. A new AE cluster, with the frequency of [400–500 kHz] observed in CAI tests of ORT-baseline and ORT-single impact specimens, was assigned to z-binding yarns fiber breakage and it was validated by the DIC results.

This study demonstrated the potential of AE for identification of different damage mechanisms in NCF, 2D and 3D woven composites under CAMI loading condition.

CRediT authorship contribution statement

Milad Saeedifar: Conceptualization, Methodology, Investigation, Formal analysis, Writing - original draft, Writing - review & editing. **Mohamed Nasr Saleh:** Conceptualization, Methodology, Investigation, Formal analysis, Writing - original draft, Writing - review & editing. **Hassan M. El-Dessouky:** Methodology, Investigation, Writing - review & editing. **Sofia Teixeira De Freitas:** Conceptualization, Supervision, Writing - review & editing. **Dimitrios Zarouchas:** Conceptualization, Supervision, Writing - review & editing.

Declaration of Competing Interest

The authors declare that they have no known competing financial interests or personal relationships that could have appeared to influence the work reported in this paper.

References

[1] Saleh MN, Soutis C. Recent advancements in mechanical characterisation of 3D woven composites. Mech Adv Mater Modern Process. 2017;3(1):12.
[2] Richardson MOW, Wisheart MJ. Review of low-velocity impact properties of composite materials. Compos A Appl Sci Manuf 1996;27(12):1123–31.
[3] Greve L, Pickett AK. Delamination testing and modelling for composite crash simulation. Compos Sci Technol 2006;66(6):816–26.
[4] Hart KR, Chia PXL, Sheridan LE, Wetzel ED, Sottos NR, White SR. Mechanisms and characterization of impact damage in 2D and 3D woven fiber-reinforced composites. Compos A Appl Sci Manuf 2017;101:432–43.
[5] Hart KR, Chia PXL, Sheridan LE, Wetzel ED, Sottos NR, White SR. Comparison of Compression-After-Impact and Flexure-After-Impact protocols for 2D and 3D woven fiber-reinforced composites. Compos A Appl Sci Manuf 2017;101:471–9.
[6] Saleh MN, El-Dessouky HM, Saeedifar M, De Freitas ST, Scaife RJ, Zarouchas D. Compression after multiple low velocity impacts of NCF, 2D and 3D woven composites. Compos A Appl Sci Manuf 2019;125:105576.
[7] Seltzer R, González C, Muñoz R, Llorca J, Blanco-Varela T. X-ray microtomography analysis of the damage micromechanisms in 3D woven composites under low-velocity impact. Compos A Appl Sci Manuf 2013;45:49–60.
[8] Sánchez DM, Gresil M, Soutis C. Distributed internal strain measurement during composite manufacturing using optical fibre sensors. Compos Sci Technol 2015;120:49–57.
[9] Hao W, Yuan Z, Tang C, Zhang L, Zhao G, Luo Y. Acoustic emission monitoring of damage progression in 3D braiding composite shafts during torsional tests. Compos Struct 2019;208:141–9.
[10] Zhang P-f, Zhou W. Yin H-f, Shang Y-j. Progressive damage analysis of three-dimensional braided composites under flexural load by micro-CT and acoustic emission. Compos Struct 2019;226:111196.
[11] Ng CT, Veidt M. A Lamb-wave-based technique for damage detection in composite laminates. Smart Mater Struct 2009;18(7):074006.
[12] Saeedifar M, Mansvelder J, Mohammadi R, Zarouchas D. Using passive and active acoustic methods for impact damage assessment of composite structures. Compos Struct 2019;226:111252.
[13] Li Z, Haigh AD, Saleh MN, McCarthy ED, Soutis C, Gibson AAP, et al. Detection of Impact Damage in Carbon Fiber Composites Using an Electromagnetic Sensor. Res Nondestr Eval 2018;29(3):123–42.
[14] Saleh MN, Yudhanto A, Lubineau G, Soutis C. The effect of z-binding yarns on the electrical properties of 3D woven composites. Compos Struct 2017;182:606–16.
[15] Saeedifar M, Fotouhi M, Ahmadi Najafabadi M, Hosseini Toudeshky H. Prediction of delamination growth in laminated composites using acoustic emission and Cohesive Zone Modeling techniques. Compos Struct 2015;124:120–7.
[16] Yousefi J, Mohamadi R, Saeedifar M, Ahmadi M, Hosseini-Toudeshky H. Delamination characterization in composite laminates using acoustic emission features, micro visualization and finite element modeling. J Compos Mater 2015;50(22):3133–45.
[17] Refahi Oskouei A, Ahmadi M. Acoustic Emission Characteristics of Mode I Delamination in Glass/Polyester Composites. J Compos Mater 2010;44(7):793–807.
[18] Refahi Oskouei A, Heidary H, Ahmadi M, Farajpur M. Unsupervised acoustic emission data clustering for the analysis of damage mechanisms in glass/polyester composites. Mater Des 2012;37:416–22.
[19] Fotouhi M, Pashmforoush F, Ahmadi M, Refahi Oskouei A. Monitoring the initiation and growth of delamination in composite materials using acoustic emission under quasi-static three-point bending test. J Reinf Plast Compos 2011;30(17):1481.
[20] Pashmforoush F, Fotouhi M, Ahmadi M. Damage Characterization of Glass/Epoxy Composite Under Three-Point Bending Test Using Acoustic Emission Technique. J of Materi Eng and Perform. 2012;21(7):1380–90.
[21] Yousefi J, Najfabadi MA, Toudeshky HH, Akhlaghi M. Damage evaluation of laminated composite material using a new acoustic emission Lamb-based and finite element techniques. Appl Compos Mater 2018;25(5):1021–40.
[22] Fotouhi M, Ahmadi Najafabadi M. Investigation of the mixed-mode delamination in polymer-matrix composites using acoustic emission technique. J Reinf Plast Compos 2014;33(19):1767–82.
[23] Saeedifar M, Fotouhi M, Najafabadi MA, Toudeshky HH. Interlaminar Fracture Toughness Evaluation in Glass/Epoxy Composites Using Acoustic Emission and Finite Element Methods. J Materi Eng Perform 2015;24(1):373–84.
[24] Arumugam V, Shankar RN, Sridhar BTN, Stanley AJ. Ultimate Strength Prediction of Carbon/Epoxy Tensile Specimens from Acoustic Emission Data. J Mater Sci Technol 2010;26(8):725–9.
[25] Arumugam V, Suresh Kumar C, Santulli C, Sarasini F, Joseph Stanley A. A Global Method for the Identification of Failure Modes in Fiberglass Using Acoustic Emission. J Test Eval 2011;39(5).
[26] Al-Jumaili SK, Holford KM, Eaton MJ, McCrory JP, Pearson MR, Pullin R. Classification of acoustic emission data from buckling test of carbon fibre panel using unsupervised clustering techniques. Struct Health Monitor 2014;14(3):241–51.
[27] Aoki Y, Suemasu H, Ishikawa T. Damage propagation in CFRP laminates subjected to low velocity impact and static indentation. Adv Compos Mater 2007;16(1):45–61.
[28] Saeedifar M, Najafabadi MA, Zarouchas D, Toudeshky HH, Jalalvand M. Clustering of interlaminar and intralaminar damages in laminated composites under indentation loading using acoustic emission. Compos B Eng 2018;144:206–19.
[29] Boominathan R, et al. Acoustic emission characterization of the temperature effect on falling weight impact damage in carbon/epoxy laminates. Compos B Eng 2014;56:591–8.
[30] Sung DU, Kim CG, Hong CS. Monitoring of impact damages in composite laminates using wavelet transform. Compos B Eng 2002;33:35–43.
[31] Saeedifar M, Najafabadi MA, Zarouchas D, Toudeshky HH, Jalalvand M. Barely visible impact damage assessment in laminated composites using acoustic emission. Compos B Eng 2018;152:180–92.
[32] Suresh Kumar C, Fotouhi M, Saeedifar M, Arumugam V. Acoustic emission based investigation on the effect of temperature and hybridization on drop weight impact and post-impact residual strength of hemp and basalt fibres reinforced polymer composite laminates. Compos B Eng 2019;173:106962.
[33] Li L, Swolfs Y, Straumit I, Yan X, Lomov SV. Cluster analysis of acoustic emission signals for 2D and 3D woven carbon fiber/epoxy composites. J Compos Mater 2015;50(14):1921–35.
[34] Li L, Lomov SV, Yan X, Carvelli V. Cluster analysis of acoustic emission signals for 2D and 3D woven glass/epoxy composites. Compos Struct 2014;116:286–99.
[35] Lomov SV, Karahan M, Bogdanovich AE, Verpoest I. Monitoring of acoustic emission damage during tensile loading of 3D woven carbon/epoxy composites. Text Res J 2014;84(13):1373–84.
[36] Tableau N, Aboura Z, Khellil K, Laurin F, Schneider J. Multiaxial loading on a 3D woven carbon fiber reinforced plastic composite using tensile-torsion tests : Identification of the first damage envelope and associated damage mechanisms. Compos Struct 2019;227:111305.
[37] Tabrizi IE, Khan RMA, Massarwa E, Zanjani JSM, Ali HQ, Demir E, et al. Determining tab material for tensile test of CFRP laminates with combined usage of digital image correlation and acoustic emission techniques. Compos A Appl Sci Manuf 2019;127:105623.
[38] Oz FE, Ersoy N, Mehdikhani M, Lomov SV. Multi-instrument in-situ damage monitoring in quasi-isotropic CFRP laminates under tension. Compos Struct 2018;196:163–80.
[39] Yuan Y, Wang S. Measurement of the energy release rate of compressive failure in composites by combining infrared thermography and digital image correlation. Compos A Appl Sci Manuf 2019;122:59–66.
[40] Ali HQ, Emami Tabrizi I, Khan RMA, Tufani A, Yildiz M. Microscopic analysis of failure in woven carbon fabric laminates coupled with digital image correlation and acoustic emission. Compos Struct 2019;230:111515.
[41] El-Dessouky HM, Saleh MN. 3D Woven Composites: From Weaving to Manufacturing. In: Rita Khanna R, Cayumil R, editors. Recent Developments in the Field of Carbon Fibers: IntechOpen; 2018. p. 51-66.
[42] International A. D7136/D7136M-15, Standard Test Method for Measuring the Damage Resistance of a Fiber-Reinforced Polymer Matrix Composite to a Drop-Weight Impact Event. West Conshohocken, PA.: ASTM International; 2015.
[43] International A. ASTM D7137 / D7137M - 17, Standard Test Method for Compressive Residual Strength Properties of Damaged Polymer Matrix Composite Plates. West Conshohocken, PA.: ASTM International; 2017.
[44] International A. ASTM E976–10, Standard guide for determining the reproducibility of acoustic emission sensor response. West Conshohocken, PA.: ASTM International; 2010.
[45] Gutkin R, Green CJ, Vangrattanachai S, Pinho ST, Robinson P, Curtis PT. On acoustic emission for failure investigation in CFRP: Pattern recognition and peak frequency analyses. Mech Syst Sig Process 2011;25(4):1393–407.
[46] de Groot PJ, Wijnen PAM, Janssen RBF. Real-time frequency determination of acoustic emission for different fracture mechanisms in carbon/epoxy composites. Compos Sci Technol 1995;55(4):405–12.
[47] Gao A, Gu Y, Wu Q, Yuan C, Li M, Zhang Z. Influence of processing temperature on interfacial behavior of HKT800 carbon fiber with BMI and epoxy matrices. Chin J Aeronaut 2015;28(4):1255–62.
[48] Cristianini N, Shawe-Taylor J. An Introduction to Support Vector Machines and Other Kernel-based Learning Methods. Cambridge: Cambridge University Press; 2000.